Xylose Isomerase in Substrate and Inhibitor Michaelis States: Atomic Resolution Studies of a Metal-Mediated Hydride Shift†,‡

Timothy D. Fenn, Dagmar Ringe, and Gregory A. Petsko*

Departments of Biochemistry and Chemistry and Graduate Program in Biophysics, Rosenstiel Basic Medical Sciences Research Center, Brandeis University, Waltham, Massachusetts 02454-9110

Received January 27, 2004; Revised Manuscript Received March 31, 2004

ABSTRACT: Xylose isomerase (E.C. 5.3.1.5) catalyzes the interconversion of aldose and ketose sugars and has an absolute requirement for two divalent cations at its active site to drive the hydride transfer rates of sugar isomerization. Evidence suggests some degree of metal movement at the second metal site, although how this movement may affect catalysis is unknown. The 0.95 Å resolution structure of the xylitol-inhibited enzyme presented here suggests three alternative positions for the second metal ion, only one of which appears positioned in a catalytically competent manner. To complete the reaction, an active site hydroxyl species appears appropriately positioned for hydrogen transfer, as evidenced by precise bonding distances. Conversely, the 0.98 Å resolution structure of the enzyme with glucose bound in the α-pyranose state only shows one of the metal ion conformations at the second metal ion binding site, suggesting that the linear form of the sugar is required to promote the second and third metal ion conformations. The two structures suggest a strong degree of conformational flexibility at the active site, which seems required for catalysis and may explain the poor rate of turnover for this enzyme. Further, the pyranose structure implies that His53 may act as the initial acid responsible for ring opening of the sugar to the aldose form, an observation that has been difficult to establish in previous studies. The glucose ring also appears to display significant segmented disorder in a manner suggestive of ring opening, perhaps lending insight into means of enzyme destabilization of the ground state to promote catalysis. On the basis of these results, we propose a modified version of the bridged bimetallic mechanism for hydride transfer in the case of *Streptomyces olivochromogenes* xylose isomerase.

Xylose isomerase catalyzes the interconversion of several aldose and ketose sugars and thus represents a major constituent in sugar metabolism. The enzyme-catalyzed interconversion of these sugars involves isomerization between an α-hydroxy aldehyde and an α-hydroxy ketone through a formal transfer of two hydrogens. The general mechanism involves transfer of one hydrogen as a proton via a catalytic base from O2 to O1 (in the aldose to ketose direction; Scheme 1), while the second hydrogen transfer can occur in two mechanistically distinct forms. The first requires proton transfer from C2 to C1 through an ene-diol intermediate, such as occurs with triose phosphate isomerase (TIM,[1] E.C. 5.3.1.1) (*1*), while the second involves direct transfer of a hydride ion (as shown in Scheme 1). Xylose isomerase carries out the latter (*2*−*7*) and primarily catalyzes the interconversion of xylose to xylulose and glucose to fructose. These sugars not only serve crucial metabolic roles but also are important commercially; hence, xylose isomerase is used for the industrial production of high fructose corn syrup.

Scheme 1: Generalized Hydride Shift Mechanism for Aldose−Ketose Sugar Interconversion[a]

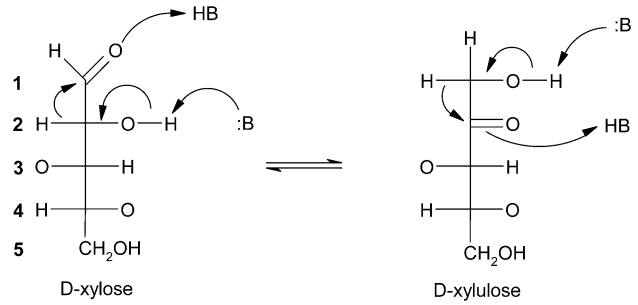

[a] Atom numbering scheme is shown in bold. Xylitol is similar to xylose with the exception that xylitol is fully reduced at the carbonyl position.

Xylose isomerase from *Streptomyces olivochromogenes* is a tetrameric enzyme containing a bridged bimetallic system that acts as an electrophilic center to promote hydride transfer

† This work was supported by USPHS Grants GM 32415 and GM 26788 to D. Ringe and G. A. Petsko. Use of the Advanced Photon Source was supported by the U.S. Department of Energy, Basic Energy Sciences, Office of Science, under Contract No. W-31-109-Eng-38. Use of the BioCARS Sector 14 was supported by the National Institutes of Health, National Center for Research Resources, under Grant Number RR07707.

‡ Coordinates and structure factors have been deposited in the RCSB Protein Data bank (http://www.rcsb.org) under the accession codes 1S5M (glucose) and 1S5N (xylitol).

* Corresponding author. Phone: (781) 736-4903. Fax: (781) 736-2405.E-mail address: petsko@brandeis.edu.

[1] Abbreviations: ADP, anisotropic displacement parameter; CSD, Cambridge Structural Database; EPR, electron paramagnetic resonance; ESD, estimated standard deviation; HEPES, *N*-(2-hydroxyethyl) piperazine-*N*′-(2-ethanesulfonic acid); NADH, nicotinamide adenine dinucleotide (reduced form); SDH, sorbitol dehydrogenase; TIM, triose phosphate isomerase; $\mathbf{U}_{eq}$, equivalent isotropic displacement tensor.

10.1021/bi049812o CCC: $27.50
Published on Web 05/05/2004

at the active site (*7*, *8*). Before doing so, evidence suggests the enzyme binds and opens the α form of the pyranose ring, although the residue(s) involved in ring opening has not been rigorously identified. Several possibilities have been put forth, including a histidine (His53), a lysine (Lys182), an aspartate (Asp286), and an activated water species (*3*, *4*, *9*−*14*). Following the ring opening step, deprotonation at O2 is believed to occur via a hydroxyl ion bound to metal ion 2 (M2) (*9*, *15*, *16*). At some point during this process, M2 shifts anywhere from 1.0 to 1.8 Å (*3*, *9*, *12*, *17*, *18*) in the direction of substrate. This second M2 position (which is now within liganding distance with substrate), in conjunction with metal ion 1 (M1), acts as the major electron withdrawing force on the substrate C−O bond from which the hydride will be transferred. This polarization leads to a partial positive character on C1, thereby reducing the energetic barrier for hydride transfer (*6*, *11*, *15*).

The rate of enzymatic isomerization via hydride transfer in the presence of magnesium ion is 5 orders of magnitude slower ($k_{cat}/K_M = 10^3$ $M^{-1}\cdot s^{-1}$ in *Streptomyces* sp. xylose isomerase (*19*)) than proton transfer by TIM, which approaches the diffusion controlled limit ($k_{cat}/K_M = 10^8$ $M^{-1}\cdot s^{-1}$ (*20*)). In this case a popular assumption is contradicted, namely, that enzymes having evolved different mechanisms yet carrying out the same overall chemistry will have comparable rates. Solution chemistry suggests that nonenzymatic hydride versus proton transfer rates are comparable ($\sim 10^{-5}$ $M^{-1}\cdot s^{-1}$), and thus, similar enzymatic rates should be achievable (*21*). Therefore, although sufficient polarization of the carbonyl group of the sugar can be provided via coordination to the metal ions of xylose isomerase, the difference in rates of catalysis for the two modes suggests a kinetic hindrance that most likely involves the rate-limiting hydride transfer step (*11*, *22*, *23*).

The disorder of the metal ion provides a possible explanation for the difference in rates because metal movement may influence free energy barriers. Also, it is unknown whether substrate has any effect on the conformational dynamics of the enzyme, for example, by shifting the energetic landscape such that metal positioning for hydride transfer is favored. However, previously determined xylose isomerase structures do not provide a detailed description of such disorder in the model due to inadequate data resolution, thereby yielding low observation-to-parameter ratios.

The advent of synchrotron radiation, cryogenic data collection methods, and sensitive diffraction counting and processing techniques allow for the collection of high-quality diffraction data. If the protein crystals are well ordered, data to true atomic resolution (<1.0 Å) may be observable. In turn, improved refinement techniques have led to the development of sophisticated models of protein disorder (*24*). In particular, atomic anisotropic displacement parameters (ADPs) can be refined given the high observation-to-parameter ratio attainable at atomic resolution. ADPs are derived from a trivariate normal distribution model of atomic disorder and therefore provide information about both the magnitude and directionality of the disorder of individual atoms in three-dimensional Cartesian space, which may be related to functional and mechanistic imperatives. ADPs can be graphically represented by defining an ellipsoid equivalent to the probability of finding the atom within the volume of the ellipsoid (for a detailed description of ADPs, see ref *25*). While Bragg diffraction data do not contain information regarding correlated atomic disorder per se, correlations in atomic displacements can often be inferred from the ADP model via inspection of the amplitudes and preferred directions of displacements within groups of atoms. Such methods employ a form of autocorrelation analysis between ADPs from two adjacent atoms (also called Rosenfield analysis (*26*)). A fundamental limitation of the ADP model is that it assumes that atoms move under the influence of a harmonic potential, which is known to be inaccurate for all covalently bonded atoms and is an especially problematic assumption in large and highly flexible molecules such as proteins.

In this study, we analyze the structure of *S. olivochromogenes* xylose isomerase on a more detailed level, in particular, the active site residues in coordination with the bridged bimetallic center. The observation of structurally distinct metal ion positions suggests that the enzymatic mechanism of xylose isomerase depends on motions that can be described using atomic resolution crystallography. The 0.95 and 0.98 Å resolution structures of xylose isomerase bound to both inhibitor (xylitol) and substrate (α-glucose) reported here are among the highest resolution obtained to date on this enzyme and have allowed for the refinement of ADPs and alternate conformers for side chain atoms. Additionally, the direct observation of hydrogen atoms has allowed for the determination of protonation states on some catalytically relevant groups. These results suggest a highly disordered second metal ion site at the active site, a finding that may explain the relatively slow rate of catalysis compared to enediol-based mechanisms. The glucose bound form of the enzyme suggests that His53 acts as the initial acid in catalyzing ring opening, although the presence of the ring form of the sugar in the structure implies either a "freezing out" effect or that ring opening is at least partially rate-limiting in the case of glucose under the conditions in these crystals.

MATERIALS AND METHODS

Protein Expression, Purification, and Crystallization. Xylose isomerase from *S. olivochromogenes* was obtained from cells generously provided by Dr. Arthur Glasfeld. Protein was overexpressed by IPTG induction of *Escherichia coli* HB101 cells containing the pX15 plasmid (*5*) at log phase ($A_{600} = 0.6-0.8$) in M9 broth and purified according to a modified version of the method of Allen et al. (*5*). Briefly, pelleted cells were resuspended in buffer (50 mM HEPES, pH 7.5, 10 mM $MgCl_2$) and lysed using a Fisher Scientific 550 sonic dismembrator equipped with a 0.25 in. flat tip. Cell lysate was spun at 15 000*g* for 20 min to pellet cell debris. The supernatant was then pooled and brought to 50% saturation with solid $(NH_4)_2SO_4$ and stirred at 4 °C for 30 min. Following centrifugation at 15 000*g* for 20 min, a second $(NH_4)_2SO_4$ cut was performed at 90% saturation, and the mixture was stirred at 4 °C for 30 min. After centrifugation at 15 000*g* for 20 min, the pellet was resuspended in a minimal amount of buffer and dialyzed against two changes of 1 L of buffer over 16 h. The dialyzed protein was then loaded on a Whatman DE-52 column (Pharmacia XK-50, 300 mL bed volume) preequilibrated with buffer. Xylose isomerase eluted after stepping from 0.225 M NaCl to 0.3 M NaCl, as determined using A_{280}, SDS−PAGE gels, and

activity assays described under Assays. Fractions containing xylose isomerase were pooled, brought to 90% saturation with $(NH_4)_2SO_4$, centrifuged at 15 000*g* for 20 min, resuspended in a minimal amount of buffer, and dialyzed as above. Protein activity was checked as described under Assays, and protein concentration was determined using the Bradford method. Purified protein was then stored as 20 μL aliquots in liquid N_2.

To avoid the potential for multiple or unidentified metal species or both at the active site, manganese was substituted into the enzyme solution prior to crystallization. Manganese was selected on the basis of its high affinity for both metal sites and relatively high level of activity in relation with other divalent cations (*19*, *27*). Metal removal was carried out by treating the enzyme with 100 mM EDTA for a period of 2 h or more, followed by enzyme assays to ensure full loss of activity. The inactivated enzyme was then passed over a Bio-Gel P-6DG (Bio-Rad) column equilibrated in Chelex-resin-treated 50 mM HEPES, pH 7.5, to remove EDTA and other potentially contaminating metals. Finally, $MnCl_2$ was added to the resulting solution to a final concentration of 10 mM, and assays were performed a second time to demonstrate restored activity.

Crystallization of xylose isomerase was achieved using the hanging drop vapor diffusion method at 25 °C. Drops contained a protein solution (15 mg/mL xylose isomerase in 50 mM HEPES, pH 7.5, supplemented with 10 mM $MnCl_2$) and mother liquor (2.1−2.35 M $(NH_4)_2SO_4$ in buffer). Drops consisted of either a 5:5, 6:4, or 7:3 ratio (μL) of protein/mother liquor. The well solution contained 700 μL of 2.1−2.35 M $(NH_4)_2SO_4$ in buffer. Crystals appeared in approximately 1 week and grew to a size of 1.0 × 0.5 × 0.5 mm^3. In an attempt to determine Michaelis complex structures, several stepwise soaks in increasing concentrations of α-D-glucose or xylitol (up to 1 M glucose or 100 mM xylitol in buffer complemented with 2.2 M $(NH_4)_2SO_4$) were performed. Crystals presoaked in glucose or xylitol were quickly passed through a 60% saturated sodium malonate solution in buffer (containing substrate or inhibitor) with a nylon loop before direct immersion in liquid N_2. All crystals tested at 100 K have the symmetry of space group *I*222.

Assays. Protein activity was monitored using a coupled sorbitol dehydrogenase (SDH) assay. The assay mix contained 25 mM HEPES, pH 7.5, 300 mM NADH, 0.45 units of SDH (1 unit will convert 1 mmol of D-fructose to D-sorbitol per minute at pH 7.6 and 25 °C), and a variable amount of substrate (20 mM xylose was used during purification). The reaction was initiated by adding the desired amount of enzyme and monitoring the decrease in absorbance at 340 nm.

Data Collection and Processing. S. olivochromogenes xylose isomerase crystallized in space group *I*222 with unit cell dimensions $a = 85.906$, $b = 92.883$, and $c = 98.321$ Å, containing one monomer per asymmetric unit. Diffraction data were collected at BioCARS at Argonne National Labs on beamline 14-BMC using a Quantum Q4 detector and 12.4 keV radiation (1.0 Å) at 100 K. To collect high angle data, the detector was offset 80 mm on the *y*-axis and moved to a crystal to detector distance of 100 mm. An initial high resolution pass was then performed in 0.5° oscillations for 180° of total data. Following this, a low resolution pass was performed with no detector offset, a reduced exposure time, and a crystal to detector distance of 150 mm. A single crystal was used for both the xylitol and glucose soak experiments. The data were processed and scaled using the HKL2000 and SCALEPACK packages, respectively. All data sets (low resolution pass to 1.3 Å resolution, high-resolution passes to 0.9 and 0.95 Å resolution in the xylitol and glucose experiments, respectively) were merged in the final SCALEPACK job with 266 806 and 229 134 unique reflections and an overall R_{merge} of 4.2% and 5.3% on intensities for the xylitol and glucose data sets, respectively. All data statistics are summarized in Table 1.

Table 1: Data Statistics[a]

	resolution	unique reflns	completeness (%)	multiplicity	$\langle I/\sigma(I)\rangle$	R_{merge}
xylitol	1.01−0.95	36 904	84.0	2.6	2.7	0.440
	50.0−0.95	234 193	92.3	4.5	25.5	0.042
glucose	1.02−0.98	20 308	83.4	2.9	2.3	0.473
	50.0−0.98	212 189	93.6	4.6	24.1	0.053

[a] Data represents combined scaling of two data sets for each crystal. Solvent content of the crystals is 37.5%, given one molecule in the asymmetric unit of the *I*222 cell.

Crystal Pseudosymmetry. Previously reported structures of *S. olivochromogenes* xylose isomerase point out its pseudo-*I*222 character resulting from a slight tilt of 2.4° along the *z*-axis between two crystallographically related monomers. As a result, those structures are refined as a dimer in the true $P2_12_12$ cell, which relates the two monomers by the noncrystallographic operator described above. However, initial refinement of the low-temperature structures reported here did not support this space group, and therefore all refinement was carried out in the *I*222 cell. It should be noted that this is the first cryogenic data collection performed with this isozyme of xylose isomerase, and the change in space group symmetry is probably a direct result of freezing conditions.

Model Refinement−CNS Refinement. Both data sets were phased using a previously solved monomeric model (to reduce it from the $P2_12_12$ to the *I*222 cell) of *S. olivochromogenes* xylose isomerase (PDB ID 1XYA) stripped of all metal ions and waters. Initial steps of the refinement were performed using all data to 1.2 Å resolution only, although the full resolution range was flagged for cross validation (5% or approximately 13 000 reflections). No sigma cutoffs were applied at any time, and refinement was carried out using a maximum likelihood amplitude-based target function with a bulk solvent correction as implemented in the Crystallography and NMR System (CNS) package (*28*, *29*). All refinement progress (including SHELX refinement, detailed below) is outlined in Table 2.

After the monomer was located in the asymmetric unit, rigid body refinement was perfomed followed by simulated annealing using torsional molecular dynamics, conjugate gradient energy minimization, and water picking. This initial model was analyzed manually in the model-building program O (*30*) using σ_A-weighted electron density maps with coefficients $F_o - F_c$ and $2F_o - F_c$ to look for side chain errors. The electron density maps showed clear evidence for metal ions and sugar in the active site, although none were added at this stage.

Model Refinement−SHELX97 Refinement. The final CNS model (R_{free} = 20.1% and 27.8%, R = 19.6% and 27.0%

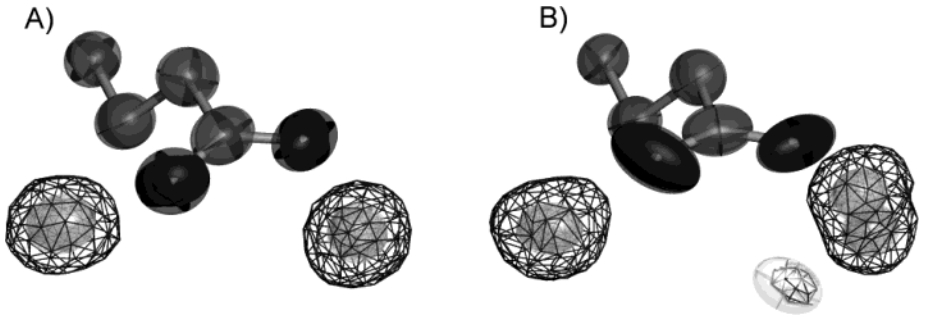

FIGURE 1: Anomalous difference electron density maps at the active site of the glucose (A) and xylitol (B) structures. Difference Fouriers were calculated using model phases prior to the inclusion of metals and are contoured at the 4σ level. The difference density at the first metal position (Mn1) is roughly spherical in both structures, suggesting only one site. The second metal position supports one and three metal positions in the glucose and xylitol structures, respectively. Glu216 is shown for orientation purposes. All atoms, unless otherwise indicated, are illustrated as ADPs at the 50% isoprobability level. All figures were generated using POVScript+ (*41*) and rendered using POVRay (http://www.povray.org).

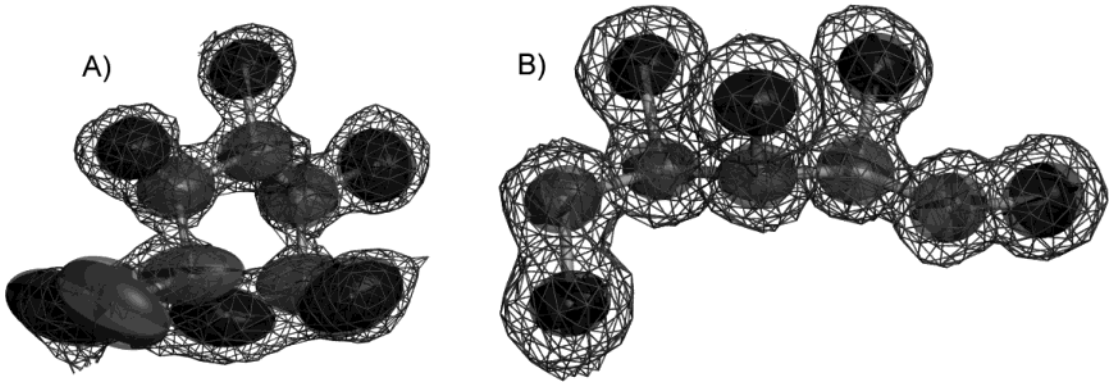

FIGURE 2: Electron density (σ_A-weighted $F_o - F_c$ maps) at the active site of the glucose (A) and xylitol (B) structures before the inclusion of the shown atoms in the refined model phases. Density is contoured at the 3σ level.

Table 2: Refinement Progress

	xylitol			glucose		
model	N_{par}	R_{work} (%)	R_{free} (%)	N_{par}	R_{work} (%)	R_{free} (%)
final CNS model, 50−1.2 Å	13 663	20.1	21.6	13 569	19.6	20.1
CNS model in SHELXL, 50−0.95/98 Å	13 663	21.4	22.9	13 569	20.0	21.0
discrete disorder modeled	14 214	20.8	22.5	14 148	19.9	20.9
ADPs added	33 044	12.7	15.0	31 807	16.5	18.6
metals, sugar added	33 383	12.5	14.8	32 024	13.0	14.8
discrete disorder modeled, solvent adjustments	34 321	12.2	14.6	32 626	12.7	14.6
riding hydrogens added	34 321	11.0	13.2	32 626	11.5	13.4
additional disorder, solvent adjustments	35 339	10.6	12.8	33 226	11.0	12.9
all data included	35 339	10.6		33 226	11.1	

for the xylitol and glucose data sets, respectively) was further refined in SHELX97-2 (*31*) using conjugate gradient least-squares minimization against an intensity-based residual target function. Initial refinement included stereochemical and displacement parameter restraints, as well as a bulk solvent correction using SWAT, so that all data from 50 to 0.95/0.98 Å resolution were included.

Initial conjugate gradient least-squares minimization was performed using a stepwise improvement in resolution (STIR). After each refinement cycle, σ_A-weighted difference electron density maps were inspected, and manual alterations were made where appropriate. Changes were applied only when both σ_A-weighted $2F_o - F_c$ ($>1\sigma$) and $F_o - F_c$ ($>2\sigma$) maps agreed and indicated an error or alternative conformer. After initial refinement, alternate conformers were modeled. The amino acid residues were restricted to have occupancies sum to unity using the FVAR instruction and allowed to refine. Following this step, anisotropic displacements were added and refined, which yielded a significant improvement in both σ_A-weighted difference electron density maps and R values (~7% and 2% in both R_{free} and R for the xylitol and glucose data sets, respectively). ADPs of protein atoms were restrained on the basis of rigid-bond (DELU) and similarity (SIMU) parameters, and solvent molecules were restrained on the basis of an approximate isotropic (ISOR) model. This step was followed by the addition and refinement of manganese ions and bound sugar/inhibitor. The number and position of the metals were based on anomalous difference Fourier syntheses (Figure 1). Also, σ_A-weighted difference electron density maps for the bound glucose and xylitol allowed for unambiguous placement of the sugars (Figure 2). The three alternative metal positions (referred to as Mn2 (a), (b), and (c)) in the xylitol structure were assigned independent free variables. All added atoms were refined isotropically for 10 rounds before generating ADPs. Further refinement rounds modeled additional alternate conformers (as well as minor adjustments to existing conformers) and solvent. The final stages of refinement included riding hydrogen atoms (placed on the basis of geometric criteria and not independently refined (*31*)) as well as a rotating hydroxyl hydrogen (to maximize agreement with the electron density, modeled using a HFIX 147 instruction), yielding a further decrease in R and R_{free} of approximately 1.2% (Table 2). The final SHELX refinement included all reflections for

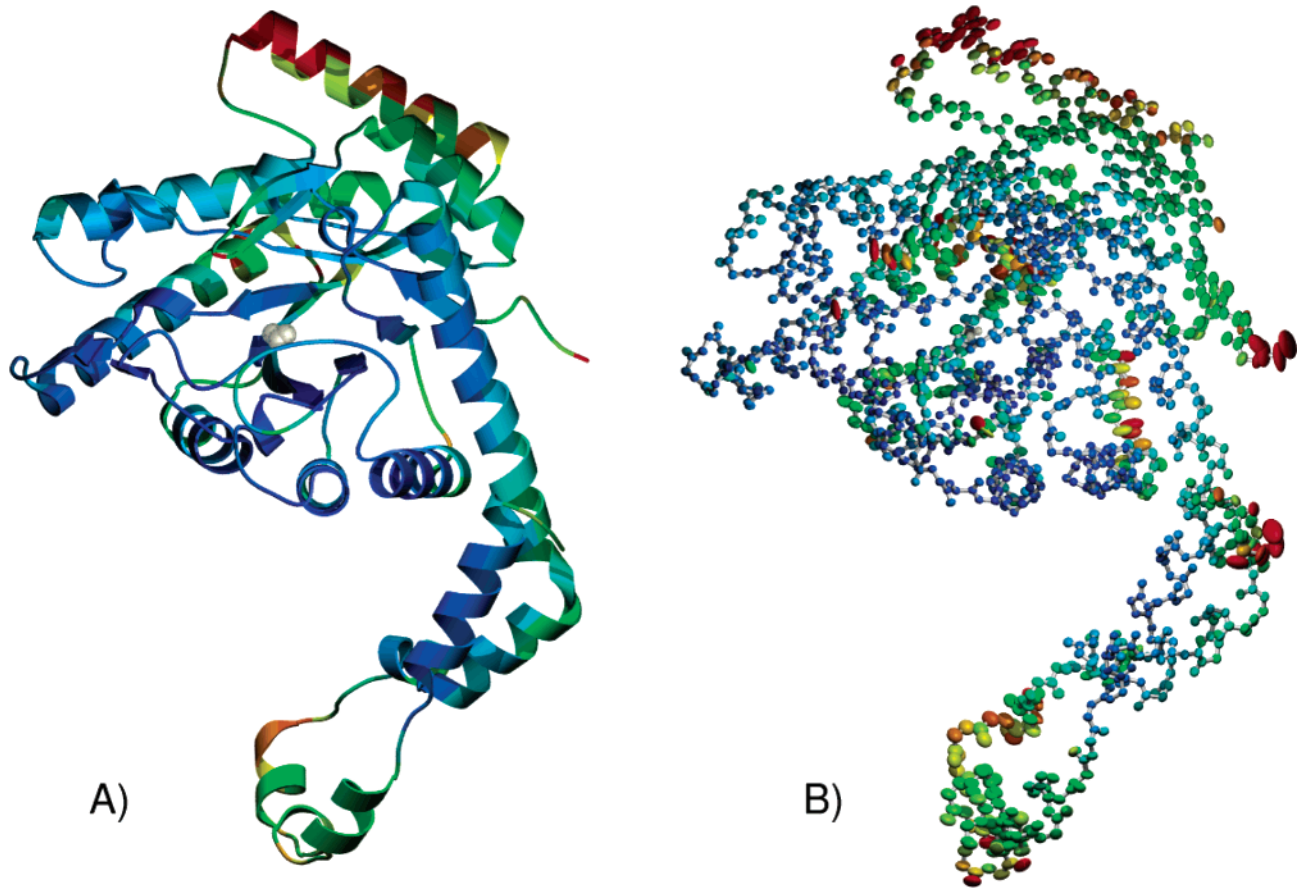

FIGURE 3: Ribbon and atomic mainchain representation of xylose isomerase, colored according to $\mathbf{U}_{eq}$ values (range is from 5 (blue) to 20 Å^2 (red)). Panel A shows the overall structure of xylose isomerase. Mn^{2+} ions are illustrated as silver spheres, located in the central portion of a TIM barrel. Panel B shows the ADP representation (mainchain atoms including alternate conformers only) of xylose isomerase. The largest anisotropy lies at the termini and crystallographically "exposed" regions (see text for discussion).

10 rounds at an observation-to-parameter ratio of approximately 7:1.

Model Quality. The final SHELX97 models (10.6% and 11.1% *R* values for xylitol and glucose, respectively) were subjected to a single round of a blocked-matrix least-squares refinement without consideration of thermal parameters (BLOC 1). This was done to generate estimated standard deviations (ESDs) for atomic positions by matrix inversion and generated the values summarized in Table 3. No residues were in disallowed regions of the Ramachandran plot, and the overall *G*-scores for the structures are 0.02 and 0.03 for xylitol and glucose, respectively (*32*).

RESULTS AND DISCUSSION

Final Model. The 0.95 Å resolution structure of xylose isomerase with xylitol bound is shown as both a ribbon and an ADP representation in Figure 3. As described previously, the overall fold is that of an eight stranded parallel α/β barrel with the active site located at the C-terminal end of the barrel. A long C-terminal extension wraps around the neighboring subunit to stabilize the dimer. The α/β barrel region of the protein is relatively well ordered, indicating a rigid active site overall, while the C-terminal and surface domains (which mostly constitute extraneous regions of the protein) exhibit a larger degree of disorder. Of more specific interest are the regions of residues 22−27 (a loop between two β-strands) and 60−80 (located in an α-helix) (indicated in Figure 3), which seem to share large directional displacements, sug-

Table 3: Model Statistics

structure	xylitol	glucose
no. of protein residues	386	386
no. of discretely disordered residues[a]	36	24
R_{work}	10.6	11.0
R_{free}	12.8	12.9
Mean ESD (Å)[b]		
protein mainchain/ side chain atoms	0.04	0.04
sugar atoms	0.01	0.03
metal positions	0.01	0.01
Mean $\mathbf{U}_{eq}$ (Å^2)[b]		
protein mainchain/ side chain atoms	0.08	0.09
sugar atoms	0.05	0.10
metal positions	0.08	0.10
Mean Anisotropy[c]		
protein mainchain/ side chain atoms	0.45	0.53
sugar atoms	0.57	0.51
metal positions	0.56	0.74

[a] Discretely disordered residues refers to amino acids that sample more than one distinct conformation with the restraint in SHELX97 that all distinct conformations for each amino acid sum to an occupancy of 1.0. [b] Mean ESD and $\mathbf{U}_{eq}$ values were determined from blocked, unrestrained full matrix least-squares minimization followed by matrix inversion as implemented in SHELX97. Hydrogen atoms were not included in the calculation. [c] Anisotropy represents the ratio of the lengths of the smallest and largest eigenvalue of the ADPs as implemented in PARVATI.

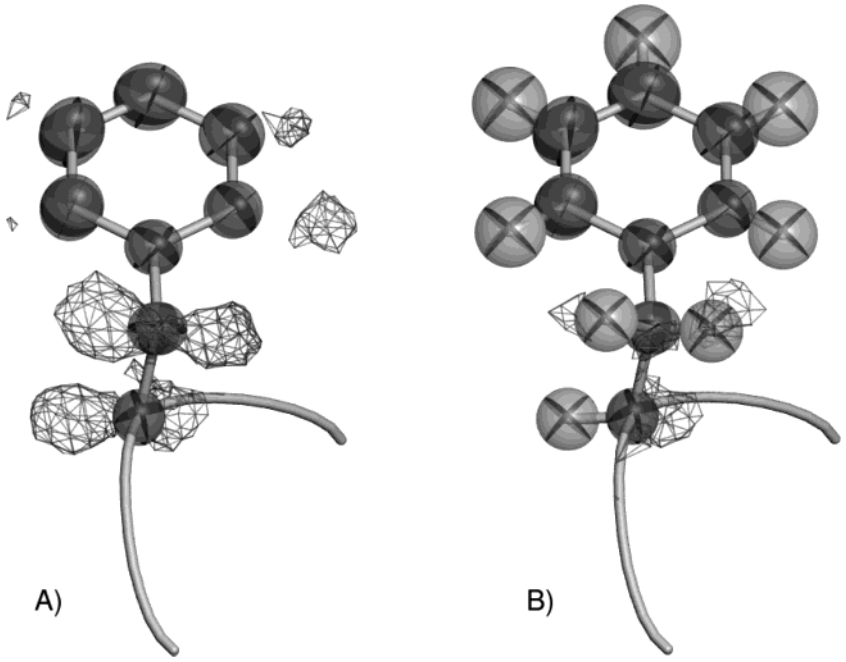

FIGURE 4: Model (Phe268) and electron density maps before and after the addition of riding hydrogens. $F_o - F_c$ maps are contoured at 2σ in both cases. In panel A, $F_o - F_c$ maps prior to implementing a riding model clearly suggest appropriate positioning of hydrogen atoms. In panel B, the final model clears up the observed difference electron density peaks, and remaining peaks appear due to slight deviations of the riding model from ideality.

gesting correlated disorder. These regions lie in portions of the protein not involved in crystal contacts with symmetry mates.

The final model includes 24 and 36 discretely disordered protein residues in the glucose and xylitol structures, respectively, or approximately 6−9% of the entire protein (Table 3). The final difference Fourier electron density maps (coefficients $F_o - F_c$) still indicate some residual density when viewed at 2σ (mostly on the surface of the protein), but none of these peaks, which appear as connected, ill-defined surfaces, could be accounted for with any certainty, and they were therefore left unmodeled. The distribution of the side chain disorder is consistent with the overall disorder noted above, that is, mostly residing on the surface and C-terminal tail of the protein. More specifically, there is some degree of bias toward solvent-exposed regions (data not shown). In some cases, residues move in subgroups; one side chain causes correlated disorder among nearby residues that is evident not only in terms of side chain−side chain interactions (via van der Waals contacts, hydrogen bonding, etc.) but also in terms of occupancies of involved residues from each group (data not shown). Some of this type of disorder is evident in the active site as well, in particular with those side chains participating in metal ion coordination (Figure 7). Although the expectation is for efficient ordering of the enzyme active site to both chemically and thermodynamically stabilize transition states and intermediates, xylose isomerase seems to sample several distinct substates (*33*, *34*). The implications of this disorder for catalysis are discussed below.

Before the addition of riding hydrogens, pronounced peaks in σ_A-weighted $F_o - F_c$ difference electron density maps at relatively well-ordered residues indicated putative protonation states. An example of this is shown in Figure 4A and, upon addition of riding hydrogens, led to the model shown in Figure 4B. It should be noted that caution is necessary in evaluating the generated hydrogen positions, because hydrogens were positioned on the basis of established geometrical criteria and refined using a riding model. The exception to this is the catalytically competent solvent hydroxyl, which was modeled with a hydrogen that was allowed to refine to maximize agreement against the electron density (HFIX 147). Therefore, the only indicator of likelihood for hydrogen positions is derived from a combination of $F_o - F_c$ electron density maps before the addition of hydrogen atoms, resulting hydrogen $\mathbf{U}_{eq}$ values from isotropic refinement, and analysis of hydrogen bonding geometry and distances with all nearby electronegative elements (HTAB).

Amino Acid Sequence. The initial sequence used for building the model was derived from the coordinates of an earlier structure of *S. olivochromogenes* xylose isomerase (PDB ID 1XYA). During the early stages of refinement, features in both the σ_A-weighted $F_o - F_c$ and $2F_o - F_c$ electron density maps suggested errors in the initial model that could not be accounted for using manual torsioning. In particular, Thr175 showed a significant ($>5\sigma$ in $F_o - F_c$ maps) peak in both the xylitol and glucose structures, approximately 1.5 Å away from the γ-carbon in a geometry that did not make chemical sense as a water molecule. This residue was checked against the corrected sequence (*35*), which contained an isoleucine at position 175. This residue fit with the experimental electron density, and all subsequent models (including the final model) contain isoleucine at position 175. All other residues were checked against the corrected sequence and verified. Only one (Arg80) was not verified, as there was no evidence for any electron density beyond the β-carbon. This residue was left in its original assignment as an alanine. The assignment of an arginine in this position may have resulted from ambiguity in the original sequencing gels (due to a rich GC base content) that led to an error in the amino acid sequence.

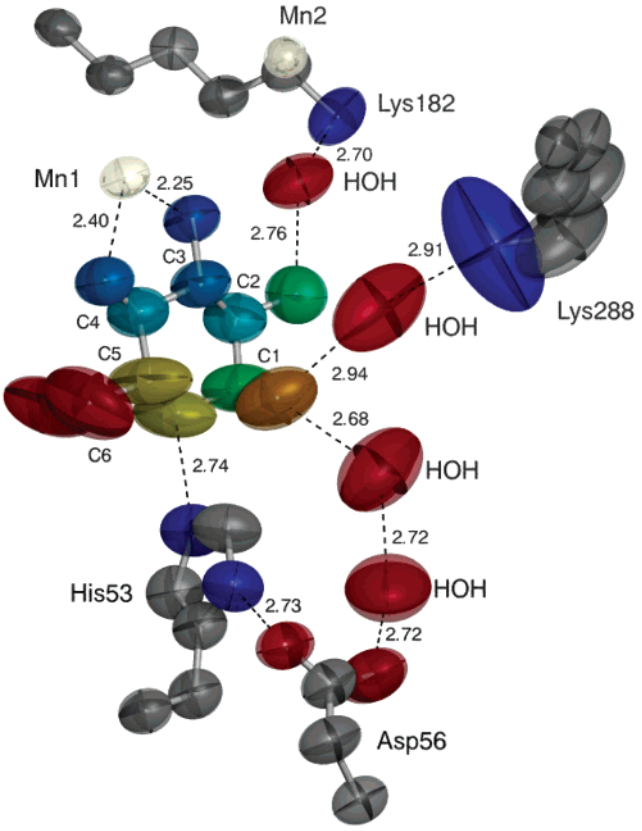

FIGURE 5: Active site of the refined glucose model structure. The glucose ring is colored according to $\mathbf{U}_{eq}$ value (range is from 10 (blue) to 20 Å^2 (red)). Hydrogen atoms are omitted for the sake of clarity. Distances are precise to within the ESDs given in Tables 3 and 4.

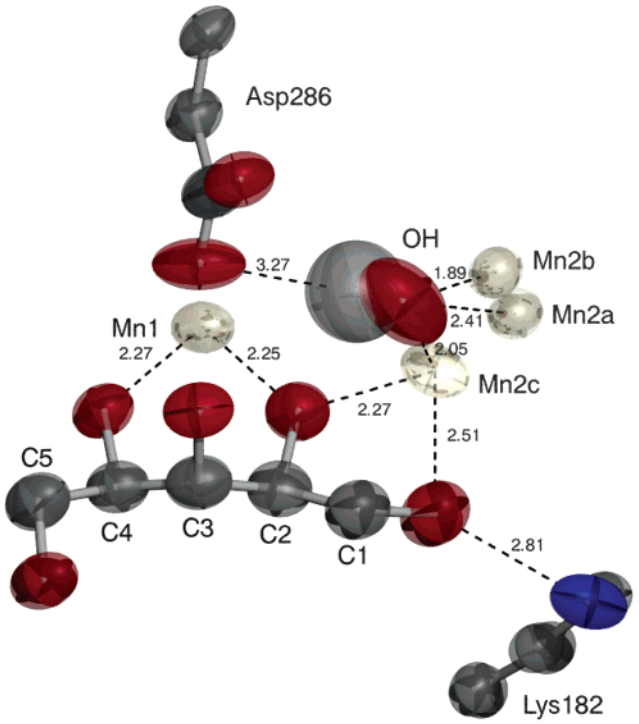

FIGURE 6: Active site of the refined xylitol model. Only the catalytic hydroxyl hydrogen is shown, generated using a rotating refinement model. Distances are significant to within the ESDs given in Tables 3 and 4.

Active Site. Residues involved in active site geometry and catalysis are shown in Figures 5−7, and ligands were determined using bond distances (Table 4) and angles about the metal centers (data not shown). Mn1 is held in the active site in a distorted octahedral configuration through ligation with the side chains of Glu180, Glu216, Asp244, Asp286, and bound sugar. To avoid steric clashes, the pyranose form of the sugar adopts a geometry such that O3 and O4 provide ligands to Mn1. In so doing, the site of ring opening (O5) is left positioned appropriately for proton donation by His53 (Figure 5). Moreover, the geometry of this interaction is such that a proton on the N_ϵ of His53 has a maximal amount of orbital overlap through the free axial electron pair of pyranose O5, thereby facilitating acid chemistry.

While His53 may be involved in chemistry at O5 of the sugar, a base is required to abstract a proton from the O1 position to generate the linear aldose form of the substrate. Although no direct interactions are apparent with O1 in the glucose structure, an intricate hydrogen bonding network is evident that implies several possibilities (Figure 5). His53, upon deprotonation, may act as a charge relay system to the neighboring Asp56, which is then hydrogen bonded to O1 through several waters. Alternatively, Lys288 may be involved via a water in proximity to O1, although the pK_a of this interaction is most likely too high to permit sufficient base catalysis. Further, the disorder inherent in Lys288 may significantly reduce any electrostatic interactions with the sugar.

Previous crystallographic and peptide mapping results have suggested His53 acts in ring opening, and the atomic resolution data presented here strongly reinforce this possibility (*3*, *12*−*14*, *36*). However, studies of H53A, H53D, and H53N mutants show that these mutations affect activity approximately 10-fold (although isomerization is still 3−4 orders of magnitude faster than solution rates of mutarotation (*37*)), while H53F, H53Y, and H53R mutations eliminate all measurable activity, suggesting a dependence on size of the introduced mutation (*4*, *10*, *23*, *38*, *39*). We propose that this phenomenon arises from an activated water species taking on the role of His53 if a large pocket is introduced by the mutation (e.g., H53A and H53D), whereas bulky side chains block this possibility and thus the ability of the enzyme to open pyranose sugars. On the basis of the mutagenic studies and the structural data reported here, we propose that His53 is the active site acid primarily involved in proton donation at O5 of the sugar and thus is critical in the ring opening step.

If the binding mode of glucose indicated here is productive, it is interesting to consider why the sugar does not isomerize. This can only be explained if the structure represents a trapped intermediate caused by the sudden freezing process prior to X-ray exposure or if ring opening is (at least) partly rate-limiting under the conditions in these crystals. Isotope effects and modeling studies suggest that hydride transfer is primarily rate-limiting, casting some doubt on the latter possibility (*11*, *22*, *23*). However, the kinetics of xylose isomerase are highly affected by the sugar substrate and metal ion composition of the enzyme, and therefore, ring opening may be partly rate-limiting under the conditions presented here (*19*, *27*).

If the binding mode observed is nonproductive, alternate means of ring opening may exist. With the use of an E180K mutant, it was shown that xylose isomerase loses the ability to bind metal ion at the M1 site (*15*), the primary ion

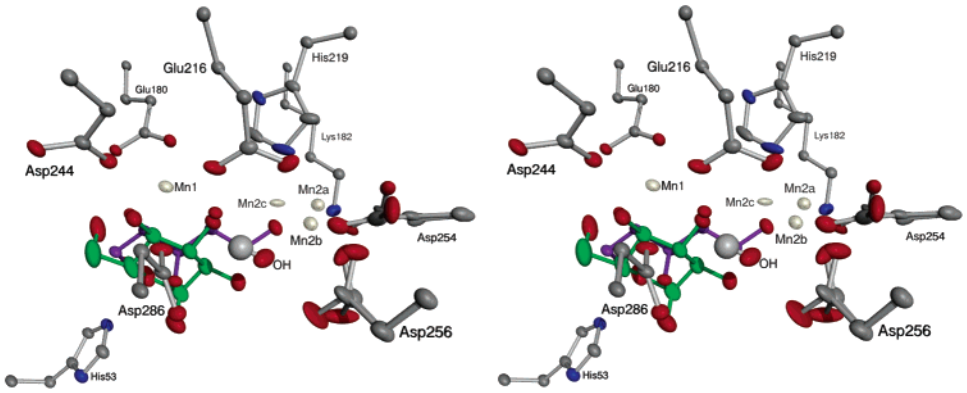

FIGURE 7: Stereoview of the active site, including all alternate side chains and metal ions. Active site residues are from the refined xylitol model with the xylitol shown in purple. The glucose structure is shown relative to the xylitol model in green. Only the catalytic hydroxyl is shown with its modeled hydrogen atom. Atoms are rendered at the 10% isoprobability level.

Table 4: Metal−Ligand Distances (Å) and Errors[a]

	xylitol				glucose	
ligand	Mn1	Mn2 (a)	Mn2 (b)	Mn2 (c)	Mn1	Mn2
180 (OE2)	2.13 (0.01)				2.10 (0.01)	
216 (OE1)	2.08 (0.01)				2.04 (0.01)	
244 (OD2)	2.10 (0.01)				2.15 (0.01)	
286 (A-OD2)	2.15 (0.01)				2.13 (0.01)	
286 (B-OD2)					2.17 (0.02)	
216 (OE2)		1.99 (0.01)	2.03 (0.01)	2.40 (0.02)		2.05 (0.01)
219 (NE2)		2.78 (0.01)		2.06 (0.01)		2.31 (0.01)
254 (A-OD1)		2.24 (0.01)	2.78 (0.01)			2.30 (0.01)
254 (B-OD1)		2.23 (0.02)	2.45 (0.03)			
254 (A-OD2)		2.18 (0.04)	2.69 (0.03)	2.74 (0.04)		2.22 (0.01)
254 (B-OD2)		1.52 (0.03)	2.01 (0.02)	2.20 (0.04)		
256 (A-OD1)		2.38 (0.03)	1.70 (0.02)			2.20 (0.01)
256 (B-OD1)		2.43 (0.04)	1.84 (0.04)			
256 (A-OD2)			2.91 (0.01)			
256 (B-OD2)			2.78 (0.05)			
(H)OH		2.41 (0.01)	1.89 (0.01)	2.05 (0.02)		2.16 (0.01)
O1				2.51 (0.02)		
O2	2.25 (0.01)			2.27 (0.02)		
O3					2.40 (0.01)	
O4	2.27 (0.01)				2.25 (0.01)	

[a] All atom fields follow the format "residue no. (conformer − atom name)" as according to the PDB standard (version 2.2).

involved in pyranose binding and coordination (Figure 5). However, this mutant still catalyzes ring opening (at a 20% slower rate compared to wild-type), suggesting that binding modes not requiring M1 are probable. Further, the lack of a reasonable means to abstract a proton from O1 in the observed structure (vide supra) suggests that only the first half of ring opening is favored. Indeed, the presence of the pyranose sugar in this structure suggests that this binding mode represents an energy "well" that causes an unfavorable thermodynamic barrier for ring opening.

A noticeable aspect of the glucose structure is the segmented disorder between the upper half of the ring (primarily coordinated by Mn1) and the more disordered lower half (Figure 5). Further, the directionality of the disorder displayed in the lower half is suggestive of extension to the linear form. Specifically, the principal axes of all of the lower half atoms are similar to that derived from rotation around the C2−C3 and C4−C3 bonds in the sugar, as would be expected for extension of the sugar to the linear form upon scission of the C1−O6 bond. This offers a compelling example of enzymatic destabilization of the ground state, because Mn1 provides for stabilization of part of the pyranose ring, while the lower half is left poorly coordinated such that ring opening is increasingly favored.

While Mn1 appears to be primarily involved in substrate binding and stabilization, Mn2 seems to play no part in the binding event, a result corroborated by kinetic studies of mutants that abolish metal binding at the second position (*15*, *17*, *39*). In the glucose bound structure, Mn2 is observed only in one position, as determined by anomalous difference electron density maps of the active site (Figure 1A). However, the xylitol structure displays three distinct metal conformations at the second metal ion site (Figure 1B), suggesting that the additional conformations require the linear form of the sugar. To compensate for this disorder, several active site residues also display alternate conformations collinear with the Mn2 displacements (Figure 7). In conformer a, the metal ion is held as a distorted octahedron via Glu216, His219, Asp254, Asp256, and the catalytic hydroxyl ion. Assignment of the protonation state of the catalytic hydroxyl is based on metal−oxygen bond distances (gathered from CSD values) and is most likely a water molecule when Mn2 occupies position a (Table 4 and Figure 6, Mn2 (a)). In conformer b, Mn2 moves to a position where it is

Scheme 2: Proposed Reaction Mechanism for *Streptomyces olivochromogenes* Xylose Isomerase[a]

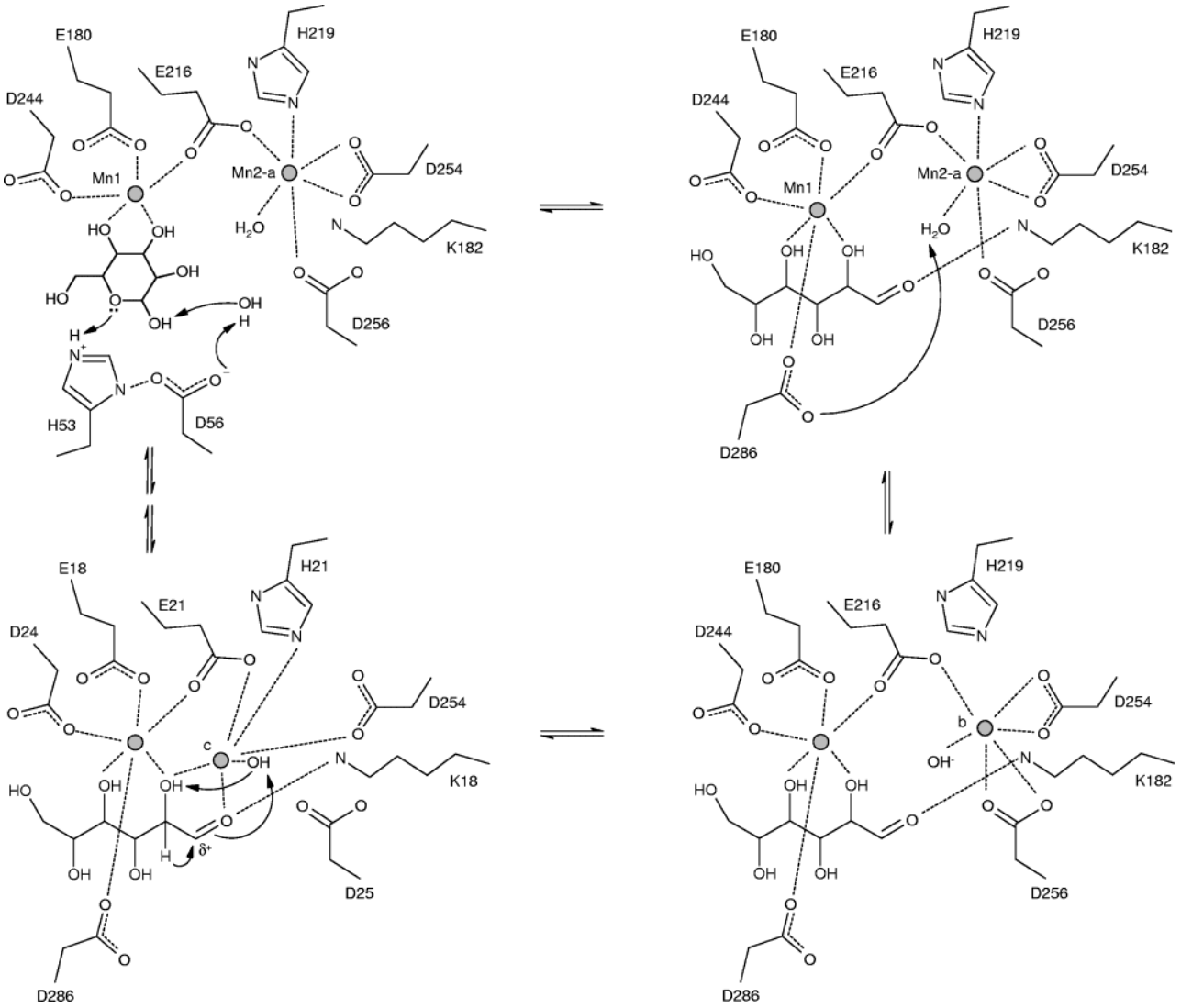

[a] If a double bond is more apparent along one bond as opposed to another (based on distances and ESDs), it is illustrated as such. Proton transfers are drawn as concerted for the sake of brevity. See text for discussion.

coordinated in a bidendate manner with Asp256 (which adopts a second conformation about the terminal carboxylate, in which it serves as a better trans ligand with Glu216 based on bond angles). Mn2 (b) is at a distance to the hydroxyl ion oxygen that is consistent with an OH− assignment (Table 4 and Figure 6, Mn2 (b)). In the third conformation (which lies 1.53 and 1.88 Å from positions a and b, respectively), which is 5-fold less occupied than the other two conformers, Mn2 loses coordination with Asp256 entirely and picks up two ligands through the bound xylitol molecule. Because this third metal position is the only conformation reasonably capable of interacting with substrate, we conclude that this conformation reflects the catalytically competent position. While the mean anisotropy for this position (0.222) differs greatly from unity (i.e., a perfectly isotropic atom), the directionality of the anisotropy suggests that the metal ion spans the O1 and O2 positions (Figure 6), although the lack of stable protein ligands in this conformation may account for this result.

There are two aspects of this third conformation of Mn2 that suggest possible reasons for the lowered rate of hydride transfer. The anisotropic character (mean anisotropy 0.222) and low occupancy (0.06) of Mn2 (c) suggest a high degree of disorder in this position, most likely reflecting the loss of coordination with a stably positioned side chain (Asp256). In this case, the electrophilicity imposed on substrate O1 by metal ion is moderate at best, resulting in a reduced partial positive charge on C1 of the sugar. This, in turn, would decrease the enzyme's effectiveness at lowering the free energy barrier for the rate-limiting hydride transfer. The presence of the reactive form of the substrate (i.e., the aldose sugar) rather than inhibitor may, however, influence the disorder at the Mn2 (c) position. EPR experiments support this possibility, because the presence of substrate produces a line-broadening effect consistent with metal movement, while xylitol shows little change in hyperfine interactions (*18*). Alternatively, the requirement of an unfavorable conformational change (Mn2 position a/b → c) for catalysis is a classical consideration for slow kinetics (*40*). In the event that the conformational change is favorable, the likelihood of achieving the third metal ion conformation will therefore be dictated by configurational entropy. Mutations that cause some of the active site residues to occupy more or less of the second metal ion pocket may also influence the confor-

mational substates of Mn2 to favor the catalytic site. Linking this information to actual enzymatic rates would provide interesting information regarding the conformational dynamics of xylose isomerase.

During the catalytic process, Lys182 is implicated in charge stabilization at O1 of bound substrate (*2*, *3*, *9*, *11*, *12*) or proton donation (*6*), and mutations at this position show no appreciable activity (*23*, *39*). Our structures suggest Lys182 is involved in binding the pyranose form of the sugar (Figure 5), as well as stabilizing the linear form for isomerization (Figure 6). The principal axes of the N_ζ ADPs for this residue appear oriented toward O1, further implicating this residue in a stabilization role.

The nature of disorder observed in the atomic resolution structures allows for the modification of the proposed reaction mechanism to that shown in Scheme 2. Residues in which double bond assignments could be clearly made (based on comparisons of bond lengths and ESDs) are illustrated as such in this scheme. Upon binding of the α-pyranose sugar, our results indicate that His53 acts in concert with Asp56 as the acid/base pair involved in ring opening. Whether an oxonium ion intermediate exists (in the event that the free electron pair on O5 deprotonates His53 in an acid-catalyzed mechanism) is still questionable. Upon ring opening and extension to the linear form, a hydroxide ion is required for the hydride shift mechanism. The rotating hydrogen refinement of the catalytic hydroxyl suggests that a hydrogen lies in line with Asp286, implying that this aspartate may act in the initial deprotonation of the water molecule bound to Mn2. However, the large degree of disorder on the refined hydrogen (Figure 6) suggests other residues could be responsible for deprotonation, such as the previously suggested Asp256 (*10*, *12*). In the case of a water species, the bonding distances (which are significant to ±0.02 Å, Tables 3 and 4) place the second manganese ion in position a, which is bidendate with Asp254. Upon generation of the hydroxyl species, Mn2 most likely adopts position b, transferring one ligand from His219 to Asp256 in the process. The presence of substrate in the aldose form and a catalytic base leads to the large metal ion shift (1.88 Å) to position c. This third metal position is the only conformation capable of inducing a positive charge on C1 of the substrate, and the disorder at this site may partly explain the oft-observed impaired kinetic parameters for the rate-limiting isomerization. The resulting imposed electrophilicity on the terminal carbonyl leads to hydride transfer complemented by hydrogen transfer via the catalytic hydroxyl. In the ketose to aldose direction, the hydride and hydrogen transfers are simply reversed; all involved catalytic ions and residues remain the same.

Atomic resolution data not only provide structural clues to atomic motions during catalysis but also can be used for descriptive computational approaches. Alternate conformers, protonation states, and displacements with magnitude and directionality terms, each with well-defined parameters, allow for in-depth analyses using QM/MM models and detailed electrostatics. Such simulations may provide insight regarding the free energies associated with hydride transfer and substrate binding, as well as how metal disorder may affect catalysis. Conformational dynamics has long been considered a culprit in cases of slow kinetics, and xylose isomerase presents an ideal system to further study this phenomenon.

ACKNOWLEDGMENT

We thank Mark Wilson, Aaron Moulin, and Bill Desmarais for many helpful discussions, comments on the manuscript, and aid in processing and refinement of the data. Todd Holyoak provided help during data collection, and Michael Bolbat (BioCARS) aided in experimental setup and logistics. Arthur Glasfeld provided the HB101 strain containing the pX15 plasmid, and Erik Vogan established the purification and assay protocols.

REFERENCES

1. Rieder, S. V., and Rose, I. A. (1958) The Mechanism of the Triosephosphate Isomerase Reaction, *J. Biol. Chem. 234*, 1007−1010.
2. Collyer, C. A., and Blow, D. M. (1990) Observations of reaction intermediates and the mechanism of aldose- ketose interconversion by D-xylose isomerase, *Proc. Natl. Acad. Sci. U.S.A. 87*, 1362−1366.
3. Collyer, C. A., Henrick, K., and Blow, D. M. (1990) Mechanism for aldose-ketose interconversion by D-xylose isomerase involving ring opening followed by a 1,2-hydride shift, *J. Mol. Biol. 212*, 211−235.
4. Lee, C. Y., Bagdasarian, M., Meng, M. H., and Zeikus, J. G. (1990) Catalytic mechanism of xylose (glucose) isomerase from *Clostridium thermosulfurogenes*. Characterization of the structural gene and function of active site histidine, *J. Biol. Chem. 265*, 19082−19090.
5. Allen, K. N., Lavie, A., Farber, G. K., Glasfeld, A., Petsko, G. A., and Ringe, D. (1994) Isotopic exchange plus substrate and inhibition kinetics of D-xylose isomerase do not support a proton-transfer mechanism, *Biochemistry 33*, 1481−1487.
6. Hu, H., Liu, H., and Shi, Y. (1997) The reaction pathway of the isomerization of D-xylose catalyzed by the enzyme D-xylose isomerase: a theoretical study, *Proteins 27*, 545−555.
7. Farber, G. K., Glasfeld, A., Tiraby, G., Ringe, D., and Petsko, G. A. (1989) Crystallographic studies of the mechanism of xylose isomerase, *Biochemistry 28*, 7289−7297.
8. Suekane, M., Tamura, M., and Tomimura, C. (1978) Physicochemical and Enzymatic Properties of Purified Glucose Isomerases from *Streptomyces olivochromogenes* and *Bacillus stearothermophilus*, *Agric. Biol. Chem. 42*, 909−917.
9. Lavie, A., Allen, K. N., Petsko, G. A., and Ringe, D. (1994) X-ray crystallographic structures of D-xylose isomerase-substrate complexes position the substrate and provide evidence for metal movement during catalysis, *Biochemistry 33*, 5469−5480.
10. Meng, M., Bagdasarian, M., and Zeikus, J. G. (1993) The role of active-site aromatic and polar residues in catalysis and substrate discrimination by xylose isomerase, *Proc. Natl. Acad. Sci. U.S.A. 90*, 8459−8463.
11. Fuxreiter, M., Farkas, O., and Naray-Szabo, G. (1995) Molecular modelling of xylose isomerase catalysis: the role of electrostatics and charge transfer to metals, *Protein Eng. 8*, 925−933.
12. Whitlow, M., Howard, A. J., Finzel, B. C., Poulos, T. L., Winborne, E., and Gilliland, G. L. (1991) A metal-mediated hydride shift mechanism for xylose isomerase based on the 1.6 Å *Streptomyces rubiginosus* structures with xylitol and D-xylose, *Proteins 9*, 153−173.
13. Carrell, H. L., Glusker, J. P., Burger, V., Manfre, F., Tritsch, D., and Biellmann, J. F. (1989) X-ray analysis of D-xylose isomerase at 1.9 Å: native enzyme in complex with substrate and with a mechanism-designed inactivator, *Proc. Natl. Acad. Sci. U.S.A. 86*, 4440−4444.
14. Carrell, H. L., Hoier, H., and Glusker, J. P. (1994) Modes of Binding Substrates and their Analogues to the Enzyme D-Xylose Isomerase, *Acta Crystallogr., Sect. D: Biol. Crystallogr. 50*, 113−123.
15. Allen, K. N., Lavie, A., Glasfeld, A., Tanada, T. N., Gerrity, D. P., Carlson, S. C., Farber, G. K., Petsko, G. A., and Ringe, D. (1994) Role of the divalent metal ion in sugar binding, ring opening, and isomerization by D-xylose isomerase: replacement of a catalytic metal by an amino acid, *Biochemistry 33*, 1488−1494.
16. Schray, K. J., and Rose, I. A. (1971) Anomeric specificity and mechanism of two pentose isomerases, *Biochemistry 10*, 1058−1062.

17. Jenkins, J., Janin, J., Rey, F., Chiadmi, M., van Tilbeurgh, H., Lasters, I., De Maeyer, M., Van Belle, D., Wodak, S. J., Lauwereys, M., Stanssens, P., Mrabet, N. T., Snauwaert, J., Matthyssens, G., and Lambeir, A.-M. (1992) Protein engineering of xylose (glucose) isomerase from *Actinoplanes missouriensis.* 1. Crystallography and site-directed mutagenesis of metal binding sites, *Biochemistry 31*, 5449−5458.
18. Bogumil, R., Kappl, R., Huttermann, J., and Witzel, H. (1997) Electron paramagnetic resonance of D-xylose isomerase: evidence for metal ion movement induced by binding of cyclic substrates and inhibitors, *Biochemistry 36*, 2345−2352.
19. van Bastelaere, P., Vangrysperre, W., and Kersters-Hilderson, H. (1991) Kinetic studies of Mg(2+)-, Co(2+)- and Mn(2+)-activated D-xylose isomerases, *Biochem. J. 278*, 285−292.
20. Blacklow, S. C., Raines, R. T., Lim, W. A., Zamore, P. D., and Knowles, J. R. (1988) Triosephosphate isomerase catalysis is diffusion controlled. Appendix: Analysis of triose phosphate equilibria in aqueous solution by 31P NMR, *Biochemistry 27*, 1158−1167.
21. Nagorski, R. W., and Richard, J. P. (2001) Mechanistic imperatives for aldose-ketose isomerization in water: specific, general base- and metal ion-catalyzed isomerization of glyceraldehyde with proton and hydride transfer, *J. Am. Chem. Soc. 123*, 794−802.
22. Rangarajan, M., and Hartley, B. S. (1992) Mechanism of D-fructose isomerization by *Arthrobacter* D-xylose isomerase, *Biochem. J. 283*, 223−233.
23. Lambeir, A. M., Lauwereys, M., Stanssens, P., Mrabet, N. T., Snauwaert, J., van Tilbeurgh, H., Matthyssens, G., Lasters, I., De Maeyer, M., Wodak, S. J., Jenkins, J., Chiadmi, M., and Janin, J. (1992) Protein engineering of xylose (glucose) isomerase from *Actinoplanes missouriensis*. 2. Site-directed mutagenesis of the xylose binding site, *Biochemistry 31*, 5459−5466.
24. Wilson, M. A., and Brunger, A. T. (2000) The 1.0 Å crystal structure of Ca(2+)-bound calmodulin: an analysis of disorder and implications for functionally relevant plasticity, *J. Mol. Biol. 301*, 1237−1256.
25. Trueblood, N., Burgi, H. B., Burzlaff, H., Dunitz, J. D., Gramaccioli, C. M., Schulz, H. H., Shmueli, U., and Abrahams, S. C. (1996) Atomic Dispacement Parameter Nomenclature. Report of a Subcommittee on Atomic Displacement Parameter Nomenclature, *Acta Crystallogr. A52*, 770−781.
26. Rosenfield, R. E. J., Trueblood, N., and Dunitz, J. D. (1978) A test for rigid-body vibrations, based on a generalization of Hirshfeld's 'rigid-bond' postulate, *Acta Crystallogr. A34*, 828−829.
27. van Bastelaere, P. B., Callens, M., Vangrysperre, W. A., and Kersters-Hilderson, H. L. (1992) Binding characteristics of Mn2+, Co2+ and Mg2+ ions with several D- xylose isomerases, *Biochem. J. 286*, 729−735.
28. Adams, P. D., Pannu, N. S., Read, R. J., and Brunger, A. T. (1997) Cross-validated maximum likelihood enhances crystallographic simulated annealing refinement, *Proc. Natl. Acad. Sci. U.S.A. 94*, 5018−5023.
29. Brunger, A. T., Adams, P. D., Clore, G. M., DeLano, W. L., Gros, P., Grosse-Kunstleve, R. W., Jiang, J. S., Kuszewski, J., Nilges, M., Pannu, N. S., Read, R. J., Rice, L. M., Simonson, T., and Warren, G. L. (1998) Crystallography & NMR system: A new software suite for macromolecular structure determination, *Acta Crystallogr., Sect. D: Biol. Crystallogr. 54*, 905−921.
30. Jones, T. A., Zou, J. Y., Cowan, S. W., and Kjeldgaard, M. (1991) Improved methods for building protein models in electron density maps and the location of errors in these models, *Acta Crystallogr. A47*, 110−119.
31. Sheldrick, G. M., and Schneider, T. R. (1997) SHELXL: high-resolution refinement, in *Methods in Enzymology* (Carter, C. W. J., and Sweet, R. M., Eds.) Vol. 277, pp 319−343, Academic Press, San Diego, CA.
32. Laskowski, R. A., Moss, D. S., and Thornton, J. M. (1993) Main-chain bond lengths and bond angles in protein structures, *J. Mol. Biol. 231*, 1049−1067.
33. Albery, W. J., and Knowles, J. R. (1976) Evolution of enzyme function and the development of catalytic efficiency, *Biochemistry 15*, 5631−5640.
34. Albery, W. J., and Knowles, J. R. (1977) Efficiency and evolution of enzyme catalysis, *Angew. Chem., Int. Ed. Engl. 16*, 285−293.
35. Gerhardt, E. (1993) Gezielte Mutagenese Eines Histidinrestes im Aktiven Zentrum der D-Xylose Isomerase von *Streptomyces olivochromogenes*: Biochemische und Strukturelle Analyse der Mutante, Ph.D. Thesis, University of Heidelberg, Heidelberg, Germany.
36. Vangrysperre, W., Ampe, C., Kersters-Hilderson, H., and Tempst, P. (1989) Single active-site histidine in D-xylose isomerase from *Streptomyces violaceoruber*. Identification by chemical derivatization and peptide mapping, *Biochem. J. 263*, 195−199.
37. Bailey, J. M., Fishman, P. H., Kusiak, J. W., Mulhern, S., and Pentchev, P. G. (1971) Mutarotase (Aldose 1-Epimerase) from Kidney Cortex, in *Methods in Enzymology* (Wood, W. A., Ed.) Vol. 41, pp 471−484, Academic Press, New York.
38. Batt, C. A., Jamieson, A. C., and Vandeyar, M. A. (1990) Identification of essential histidine residues in the active site of *Escherichia coli* xylose (glucose) isomerase, *Proc. Natl. Acad. Sci. U.S.A. 87*, 618−622.
39. Whitaker, R. D., Cho, Y., Cha, J., Carrell, H. L., Glusker, J. P., Karplus, P. A., and Batt, C. A. (1995) Probing the roles of active site residues in D-xylose isomerase, *J. Biol. Chem. 270*, 22895−22906.
40. Jencks, W. P. (1969) Covalent Catalysis, *Catalysis in Chemistry and Enzymology*, pp 42−162, Dover Publications, Inc., New York.
41. Fenn, T. D., Ringe, D., and Petsko, G. A. (2003) POVScript+: a program for model and data visualization using persistence of vision raytracing, *J. Appl. Crystallogr. 36*, 944−947.

BI049812O